PERGAMON

International Journal of Solids and Structures 39 (2002) 4697–4722

INTERNATIONAL JOURNAL OF SOLIDS and STRUCTURES

www.elsevier.com/locate/ijsolstr

# Exact static solutions to piezoelectric smart beams including peel stresses. II. Numerical results, comparison and discussion

Quantian Luo, Liyong Tong *

*School of Aerospace, Mechanical and Mechatronic Engineering, The University of Sydney, NSW 2006, Australia*

Received 14 November 2001

**Abstract**

This *part* presents the numerical results, comparisons and discussion for the exact static solutions of smart beams with piezoelectric (PZT) actuators and sensors including peel stresses presented in Part I. (International Journal of Solids and Structures, 39, 4677–4695) The actuated stress distributions in the adhesive and the adhesive edge stresses varying with the thickness ratios are firstly obtained and presented. The actuated internal stress resultants and displacements in the host beam are then calculated and compared with those predicted by using the shear lag model. The stresses in the adhesive caused by an applied axial force, bending moment and shear force are calculated, and then used to compute the sensing electric charges for comparison with those predicted using the shear lag model. The numerical results are given for the smart beam with (a) one bonded PZT and (b) two symmetrically bonded PZTs, with a comparison to those predicted using the shear lag model. Novel, simple and more accurate formulas for the equivalent force and bending moment induced by applied electric field are also derived for the host beam with one PZT or two symmetrically bonded PZTs. The symmetric shear stress and the anti-symmetric peel stress components caused by a shear force are discussed. In addition, in the case of PZT edge debonding, the stress redistribution in the adhesive and the self-arresting mechanism are also investigated.
© 2002 Elsevier Science Ltd. All rights reserved.

*Keywords:* Piezoelectric actuator and sensor; Peel stress; Debonding

## 1. Introduction

In Part I of this work (Luo and Tong, 2002), the exact static solutions including the peel stress were developed for the smart beams with one bonded piezoelectric (PZT) patch or two symmetrically bonded PZT patches. In this part, we present the numerical results, comparisons and discussion. In all the numerical calculations, the following data are employed.

* Corresponding author. Tel.: +61-2-9351-6949; fax: +61-2-9351-4841.
*E-mail address:* ltong@aeromech.usyd.edu.au (L. Tong).

0020-7683/02/$ - see front matter © 2002 Elsevier Science Ltd. All rights reserved.
PII: S0020-7683(02)00384-0

PZT: $E_1 = 7 \times 10^{10}$ N/m$^2$, $e_{31} = -5.2$ N/mV, $t_1 = 0.001$ m, $L = 0.01$ m.
Adhesive layer: $E_a = 3 \times 10^9$ N/m$^2$, $G_a = 1.07 \times 10^9$ N/m$^2$, $R_{ta} = (1–50)$.
Host beam: $E_h = 7 \times 10^{10}$ N/m$^2$ $R_{ht} = (1–50)$.

These data are typical or representative of the properties of PZT4 (Robbins and Reddy, 1991), adhesive (Tong and Steven, 1999) and aluminum. Definitions of all mathematical symbols are the same as those presented in Part I. The smart beam used for calculating the numerical results is referred to Figs. 1 and 2, respectively. As the results of either symmetric or anti-symmetric, only half of the curves are plotted in most cases. In considering influences of the thickness ratios, we let that $t_1$ be equal to 1 mm. When the other value of the PZT thickness is given, the similar conclusions can also be drawn.

In this paper, firstly, the numerical results are presented for the case of a host beam with one bonded PZT and compared them with those due to Wang and Rogers (1991), whose model was based on the classic composite theory. Secondly, the results are given for the case of a host beam with two symmetrically bonded PZT patches and then compared with those predicted using the shear lag model developed by

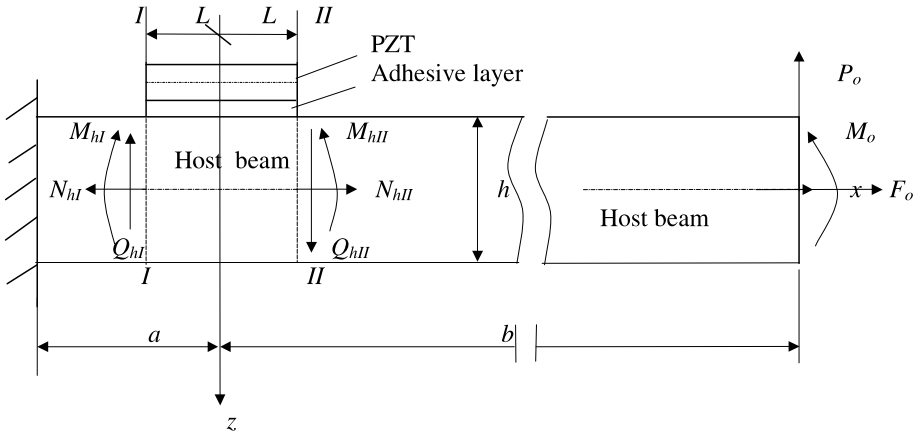


Fig. 1. A cantilever beam with one partially bonded PZT patch.

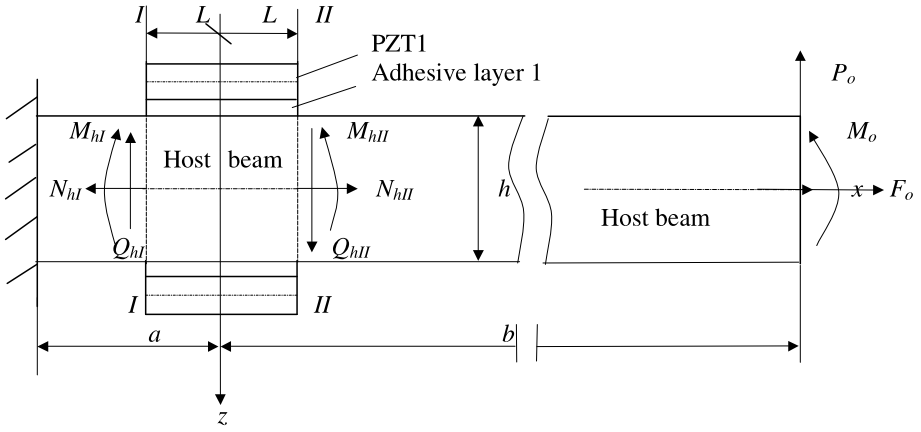


Fig. 2. A cantilever beam with two symmetrically bonded PZT patches.

Crawley and de Luis (1987). Finally, the results are compared with those obtained using the multi-segment shooting method (Tong et al., 2001).

## 2. A cantilever beam with one bonded PZT

### 2.1. PZT used as an actuator

To investigate performance of a PZT actuator, we assume that there are no applied mechanical forces on the structures and that a voltage of negative 100 V is applied to PZT shown in Fig. 1. In this case, Eq. (20) in Part I becomes:

$$H_{nk} = -r_a \varepsilon_e \quad \text{and} \quad H_{mk} = H_{qk} = 0, \qquad k = \mathrm{I}, \mathrm{II}, \quad \text{where } \varepsilon_e = -7.43\ \mu\varepsilon \tag{1}$$

Using the above materials and geometrical data and the equations given in Part I, we can calculate the non-dimensional shear and peel stresses in the adhesive layer by employing Eqs. (31) and (32) for the coupled case and Eq. (33) for the decoupled case; and we can also compute the non-dimensional internal stress resultants induced in the host beam using Eqs. (34)–(36). Both sets of non-dimensional results are presented in the following two subsections.

#### 2.1.1. Induced shear and peel stresses

Numerical results show that, over the entire length of the PZT patch, the distribution pattern of the non-dimensional shear stress is anti-symmetrical while that of the non-dimensional peel stress is symmetrical about the middle point of $\xi = 0$ (see Fig. 1). Due to this symmetrical and anti-symmetrical characteristics, Figs. 3 and 5 plot the non-dimensional shear stress $\tau_n$ along half length of the PZT patch, i.e. $0 \leqslant \xi \leqslant 1$, and Figs. 4 and 6 plot the peel stress $\sigma_n$ along 60% of half PZT length, i.e. $0.4 \leqslant \xi \leqslant 1$. As shown in Figs. 3–6, both shear and peel stresses peak at the ends of the PZT patch. It is evident that the distribution patterns of the non-dimensional shear and peel stresses over the half length of the PZT patch are similar to those observed in adhesive bonded balanced single-lap and lap-shear joints (Goland and Reissner, 1944; Tong and Steven, 1999).

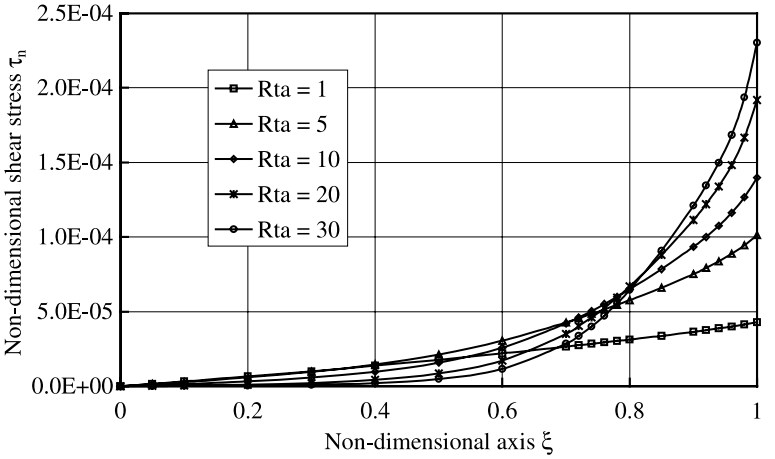


Fig. 3. Non-dimensional shear stress distribution along half of the PZT patch with $R_{ht} = 10$ and $R_{ta}$ ranging from 1 to 30.

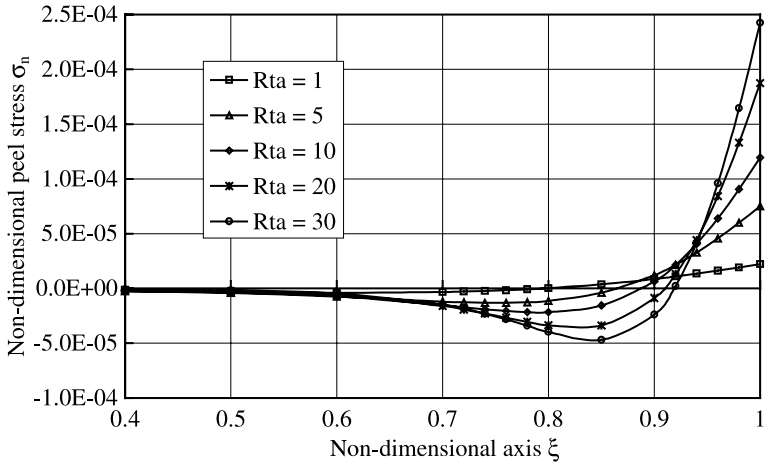


Fig. 4. Non-dimensional peel stress distribution along half of the PZT patch with $R_{ht} = 10$ and $R_{ta}$ ranging from 1 to 30.

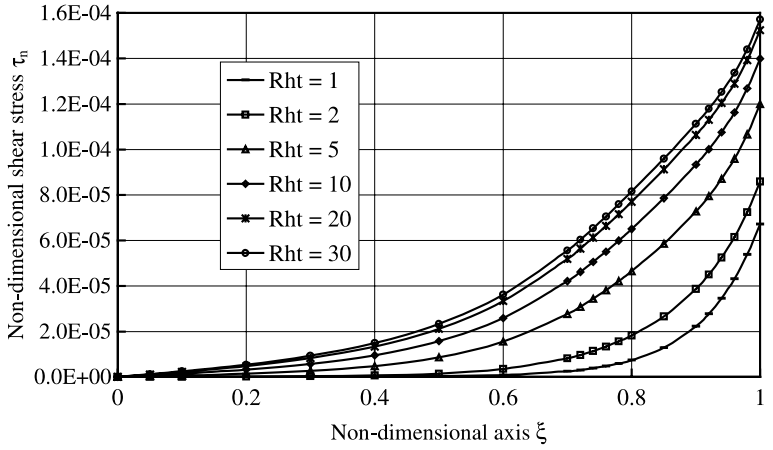


Fig. 5. Non-dimensional shear stress distribution along half of the PZT patch with $R_{ta} = 10$ and $R_{ht}$ ranging from 1 to 30.

Figs. 3 and 4 depict the stress distributions for the smart beams with a fixed host beam-to-PZT patch thickness ratio, namely $R_{ht} = 10$. The PZT patch-to-adhesive thickness ratio $R_{ta}$ varies from 1 to 30, representing a scenario when the adhesive thickness varies from the value of the PZT thickness to one 30th of the PZT thickness. It is clearly shown that, for the given material properties and thickness of the host beam and the PZT ($R_{ht} = 10$), a thinner adhesive layer tends to create larger peak shear and peel stresses while a thicker adhesive layer seems to yield smaller peak shear and peel stresses. When the PZT-to-adhesive thickness ratio $R_{ta}$ is equal to 10, 30, 50 and 100, the non-dimensional shear stresses at the edge is $1.40 \times 10^{-4}$, $2.30 \times 10^{-4}$, $2.80 \times 10^{-4}$, $3.93 \times 10^{-4}$; and the non-dimensional peel stress at the edge is $1.20 \times 10^{-4}$, $2.43 \times 10^{-4}$, $3.34 \times 10^{-4}$, $5.09 \times 10^{-4}$, respectively. This influence of the PZT-to-adhesive thickness ratio on the shear and peel stress distributions as well as their peak values is similar to that for the cases of bonded single and lap-shear joints. It is also worth noting that the peak value of the peel stress is close to that of the shear stress for large values of the PZT-to-adhesive thickness ratio, e.g. greater than 10

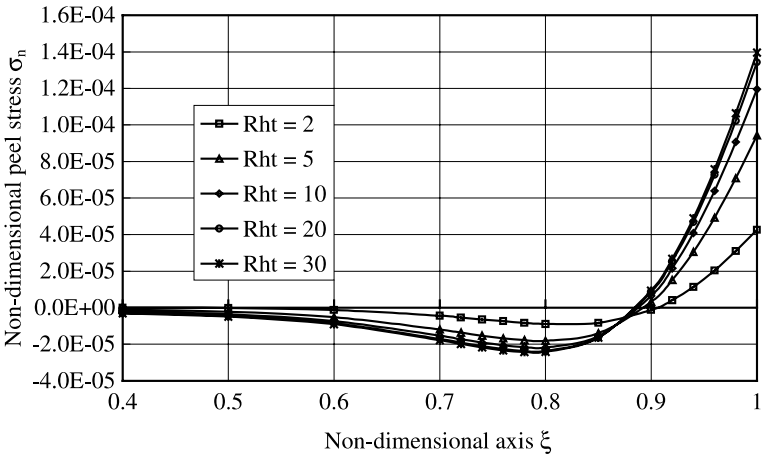


Fig. 6. Non-dimensional peel stress distribution along half of the PZT patch with $R_{ta} = 10$ and $R_{ht}$ ranging from 1 to 30.

for the considered case, although the shear stress gradient becomes steeper. However, the area under the shear stress distribution curve does not seem to change with this PZT-to-adhesive thickness ratio when it is greater than 10.

Figs. 5 and 6 show the influence of the host beam-to-PZT patch thickness ratio $R_{ht}$ on the distributions of the non-dimensional shear and peel stresses for the smart beams with a given PZT-to-adhesive thickness ratio, i.e. $R_{ta} = 10$. The host beam-to-PZT patch thickness ratio $R_{ht}$ takes values from 1 to 30. When $R_{ht} = 1$, both the host beam and PZT patch have the same thickness, which stands for the case of very flexible beam as the PZT thickness is usually less than 1 or 2 mm. When $R_{ht} = 30$, the host beam is much thicker than the PZT patch, which may represent the case of a relatively stiff beam structure. The distribution patterns for both non-dimensional shear and peel stresses are the same as those presented in Figs. 3 and 4 with their peak values at both ends of the PZT patch. As shown in Figs. 5 and 6, the peak values of the non-dimensional shear and peel stresses increase with the host beam-to-PZT patch thickness ratio $R_{ht}$, namely, the larger the thickness ratio, the greater the peak values of both non-dimensional shear and peel stresses. Similarly, as observed in Figs. 3 and 4, the peak value of the non-dimensional peel stress is in the same order as that of the non-dimensional shear stress, which may indicate the importance of the peel stress.

It is also noted that the influence of the thickness ratio $R_{ht}$ becomes less remarkable when the thickness ratio $R_{ht}$ is greater than 20. When the thickness ratio $R_{ht}$ is equal to 30, 50, 100, the peak value of the non-dimensional shear stress is $1.57 \times 10^{-4}$, $1.61 \times 10^{-4}$, $1.64 \times 10^{-4}$; and the peak value of the non-dimensional peel stress is $1.40 \times 10^{-4}$, $1.44 \times 10^{-4}$, $1.47 \times 10^{-4}$, respectively. In the relative thickness range of $R_{ht} = 30$–$100$, the differences of the peak shear and peel stresses are less than 5%.

### *2.1.2. Induced axial force, bending moment and shear force*

Figs. 7–9 depict the distributions of the non-dimensional axial force $N_{nh}$, bending moment $M_{nh}$ and shear force $Q_{nh}$ in the host beam induced by the applied electric field to the PZT patch, respectively. Due to symmetry, the three stress resultants are presented only over the domain of half PZT length. In these figures, the PZT patch-to-adhesive thickness ratio is fixed as $R_{ta} = 10$, while the host beam-to-PZT patch thickness ratio varies from 1 to 30 to show the influence of this thickness ratio on the distribution patterns and peak values of the three stress resultants.

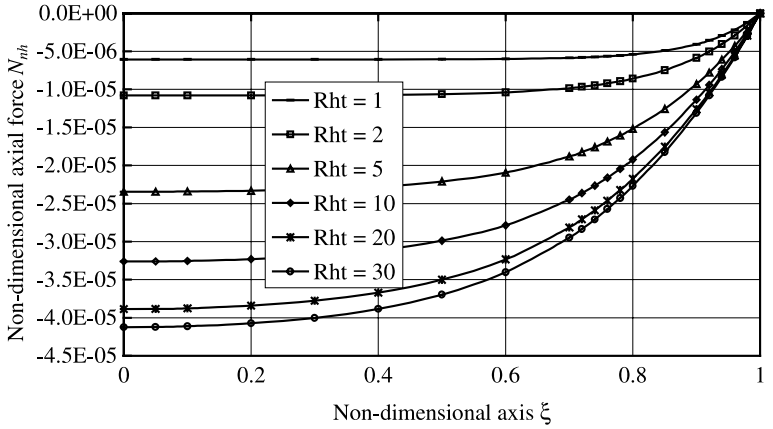


Fig. 7. Non-dimensional axial force distribution along half of the PZT patch with $R_{ta} = 10$ and $R_{ht}$ ranging from 1 to 30.

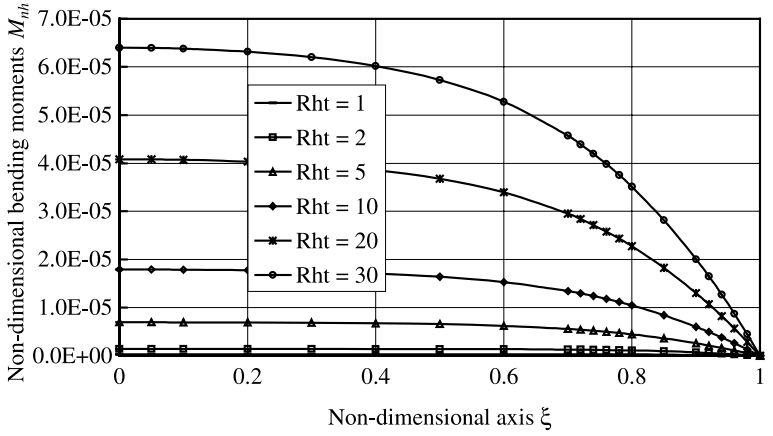


Fig. 8. Non-dimensional bending moment distribution along half of the PZT patch with $R_{ta} = 10$ and $R_{ht}$ ranging from 1 to 30.

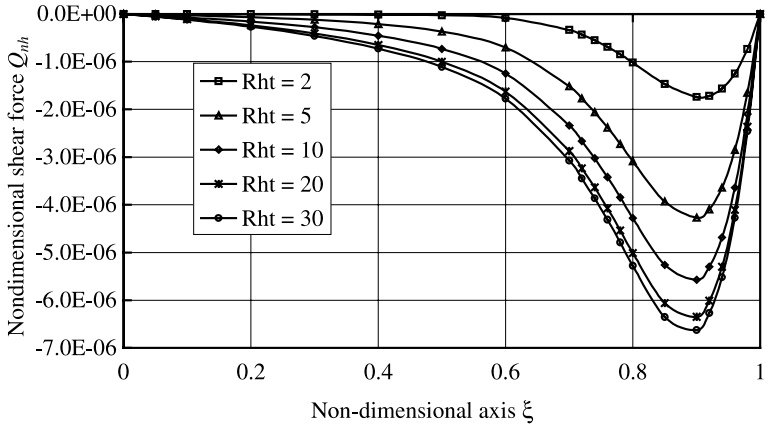


Fig. 9. Non-dimensional shear force distribution along half of the PZT patch with $R_{ta} = 10$ and $R_{ht}$ ranging from 2 to 30.

As can be seen from Figs. 7 and 8, the non-dimensional axial force and bending moment attain their maximum values at the middle point of $\xi = 0$ and become zero at the end of $\xi = 1$. For both non-dimensional induced axial force and bending moment, their absolute peak values increase when the host beam-to-PZT patch thickness ratio $R_{ht}$ is enlarged from 1 to 30. For example, when this thickness ratio $R_{ht}$ takes values of 1, 10, 20, 30, 50 and 100, the maximum axial force is $-6.07 \times 10^{-6}$, $-3.26 \times 10^{-5}$, $-3.89 \times 10^{-5}$, $-4.13 \times 10^{-5}$, $-4.33 \times 10^{-5}$ and $-4.49 \times 10^{-5}$, respectively. This can be explained, from the viewpoint of physics, that for a fixed thickness of PZT patch and fixed applied electric field, the thicker the host beam, the larger the induced axial force. However, when the induced axial forces are converted into the induced axial stresses, namely $-6.07 \times 10^{-6}$, $-3.26 \times 10^{-6}$, $-1.95 \times 10^{-6}$, $-1.38 \times 10^{-6}$, $-0.86 \times 10^{-6}$ and $-0.449 \times 10^{-6}$ for the case of $R_{ht} = 1$, 10, 20, 30, 50 and 100, respectively. Thus it can be stated that the thicker the host beam, the less the induced axial stress and strain when the thickness of the PZT patch and the applied electric field are fixed. Because the maximum bending moment component computed from the shear stress is equal to the product of the maximum axial force and the half thickness of the host beam, the bending moment component due to shear stress increases with the host beam thickness, while the corresponding maximum bending stress and curvature component decrease when the host beam thickness is increased.

As the stress concentrations occur near the edges of the PZT patch as shown in Figs. 5 and 6, the non-dimensional axial force and bending moment approach to their almost constants when moving away from the edges as depicted in Figs. 7 and 8. That is, in the middle zone covered by the PZT patch, the actuated axial force and bending moment approach to approximately constant values, which may be defined as the equivalent axial force and bending moment. As shown in Figs. 7 and 8, the host beam-to-PZT patch ratio has a remarkable influence on the size of the equivalent value zone where both the non-dimensional axial force and bending moments are approximately equal to constant. For example, the zone size is $0 \leqslant \xi \leqslant 0.8$ when $R_{ht} = 1$, $0 \leqslant \xi \leqslant 0.6$, when $R_{ht} = 2$, $0 \leqslant \xi \leqslant 0.4$ when $R_{ht} = 5$ and $0 \leqslant \xi \leqslant 0.2$ when $R_{ht} = 10$. It is clearly seen that the larger the host beam-to-PZT patch thickness ratio, the smaller the size of the equivalent value zone.

The actuated shear forces in the host beam, being the integration of the peel stress concentrating in the vicinity of the PZT patch end, is plotted versus the non-dimensional axis in Fig. 9. Similarly, the host beam-to-PZT patch thickness ratio ranges from 2 to 30 while the PZT patch-to-adhesive thickness ratio takes value of 10. Similar to the axial force and bending moment, it is noted that the larger this thickness ratio, the greater the shear force.

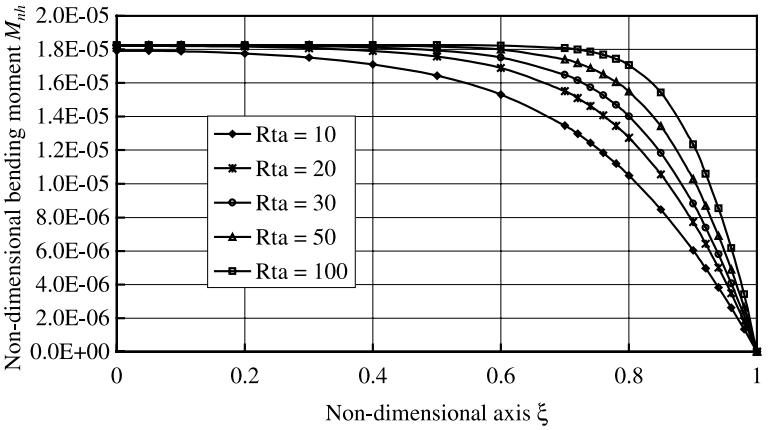


Fig. 10. Non-dimensional bending moment distribution along half of the PZT patch with $R_{ht} = 10$ and $R_{ta}$ ranging from 10 to 100.

Fig. 10 depicts the distributions of the non-dimensional bending moment $M_{nh}$ in the host beam induced by the applied electric field to the PZT patch for the smart beam with $R_{ht} = 10$ and $R_{ta}$ ranging from 10 to 100. It is found that the value of $R_{ta}$ has a negligible influence on the peak value of the non-dimensional bending moment and has a remarkable effect of the size of the equivalent zone.

Fig. 11 plots the maximum non-dimensional axial force in the host beam actuated by the applied voltage versus the PZT patch-to-adhesive layer thickness ratio when the host beam-to-PZT patch thickness ratio varies from 1 to 30. It is noted that the maximum non-dimensional axial force approaches its asymptote when the thickness ratio $R_{ta}$ increases. For the considered example, when the thickness ratio $R_{ht}$ is less than 5, the maximum non-dimensional axial force $N_{nh}$ attains its asymptote when $R_{ta}$ is larger than 5; and when $R_{ht}$ is greater than 10, $N_{nh}$ approaches its asymptote when $R_{ta}$ is larger than 10. For example, when the thickness ratio $R_{ht}$ is equal to 10, and $R_{ta}$ is equal to 10, 30, 50 and 100, the maximum non-dimensional axial force is equal to $3.26 \times 10^{-5}$, $3.32 \times 10^{-5}$, $3.32 \times 10^{-5}$ and $3.32 \times 10^{-5}$, respectively, with a relative differences less than 2%. When $R_{ta}$ is larger than 30, the curves with different values of $R_{ht}$ attain their plateaus.

Fig. 12 depicts the maximum non-dimensional bending moments $M_{nh}$ actuated in the host beam by the applied voltage when the thickness ratios $R_{ht}$ and $R_{ta}$ range from 1 to 30. It is evident that $M_{nh}$ attains its

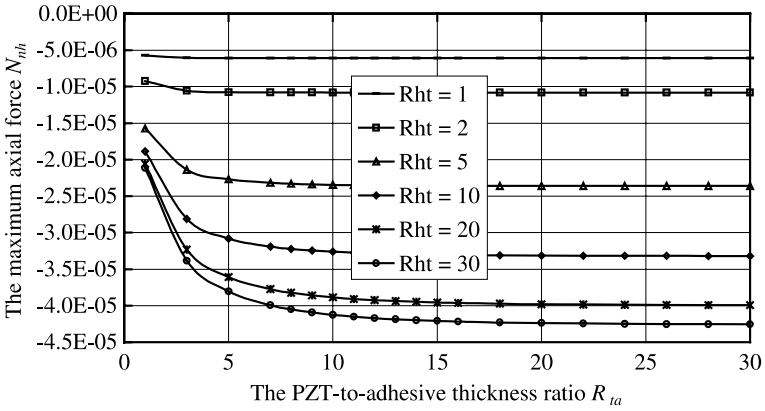


Fig. 11. The maximum axial force actuated by the applied voltage versus $R_{ta}$ with $R_{ht}$ ranging from 1 to 30.

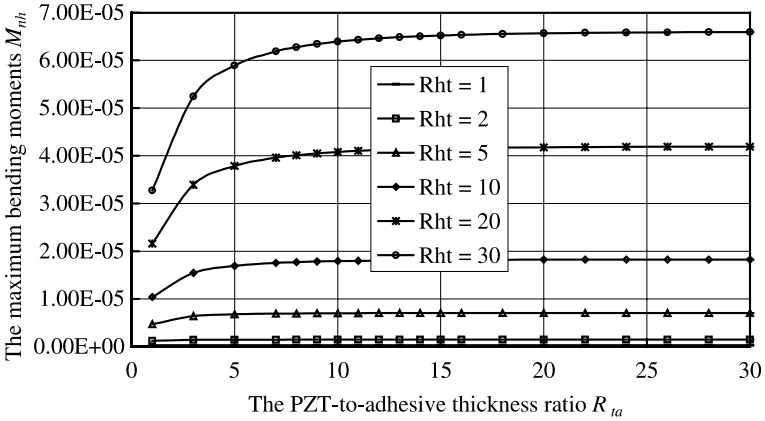


Fig. 12. The maximum bending moment actuated by the applied voltage versus $R_{ta}$ with $R_{ht}$ ranging from 1 to 30.

plateau when $R_{ta}$ is larger than 5 and the ratio $R_{ht}$ has a value less than 5, and when $R_{ta}$ is larger than 10 and the ratio of $R_{ht}$ takes a value greater than 10. As shown in Figs. 11 and 12, it can be stated that the actuated axial force and bending moment induced in the host beam are approximately independent of the thickness ratio $R_{ta}$ when it is large enough, e.g. $R_{ta} > 10$.

### 2.2. PZT worked as a sensor

The sensing electric charge is developed due to straining of the PZT sensor. We will calculate the charges caused by separately applying an axial force and a bending moment at the free end of the smart beam in Fig. 1. The sensing charge caused by a shear force is similar to that caused by the bending moment and is not given, but the shear force effects on the bonding stresses will be investigated in Section 5. The electric charges under combined loadings may be obtained by employing the superposition principle to the deformations and strains.

#### 2.2.1. Sensing charge caused by an axial force

When an axial force ($F_0$) is applied to the host beam at its free end as shown in Fig. 1, we can solve the shear and peel stresses based on the exact solutions presented in Part I (Luo and Tong, 2002). It can be shown that, the distribution patterns of the shear and peel stresses due to the applied axial force are the same as those due to the applied voltage. To investigate the parametric effects on the sensing charges, let us assume $\varepsilon_n = -7.43\ \mu\varepsilon$. This assumption means that the applied axial force is varied with the thickness of the host beam so that the strain applied to the host beam at the section where PZT patch ends remains constant. In this case, Eq. (45) in Part I is

$$H_{nk} = -r_a \varepsilon_n \quad \text{and} \quad H_{mk} = H_{qk} = 0, \qquad k = \mathrm{I}, \mathrm{II} \tag{2}$$

Substituting Eq. (2) into the equations given in the Appendix of Part I, we can determine the integration constants and then obtain the sensing electric charges. Fig. 13 depicts the sensing charge $q_n$ versus the thickness ratio $R_{ht}$ ranging from 1 to 50 with the thickness ratio $R_{ta}$ varying from 1 to 30. Fig. 13 shows that the thinner the adhesive layer, the larger the sensing electric charge. However, it should be pointed out that the electric charge increases only slightly with a thinning adhesive layer when the thickness ratio $R_{ta}$ is larger than 10. The sensing electric charge increases with the thickness ratio $R_{ht}$ and approaches to an asymptote, and it also increases with the thickness ratio $R_{ta}$ as well as attains its asymptote.

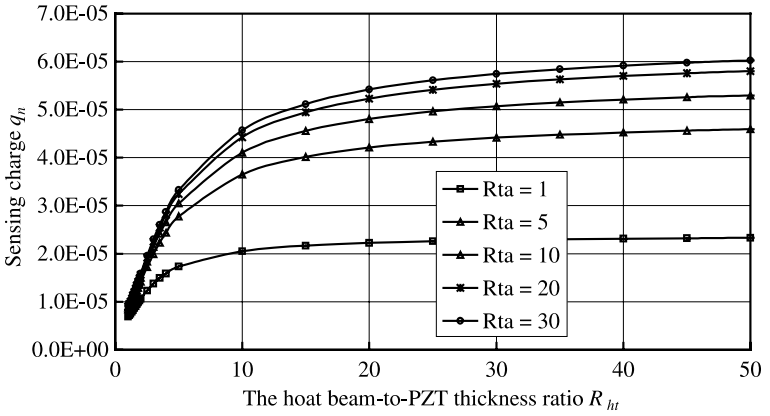


Fig. 13. Sensing charges ($q_n$) caused by the axial force versus $R_{ht}$ with $R_{ta}$ ranging from 1 to 30.

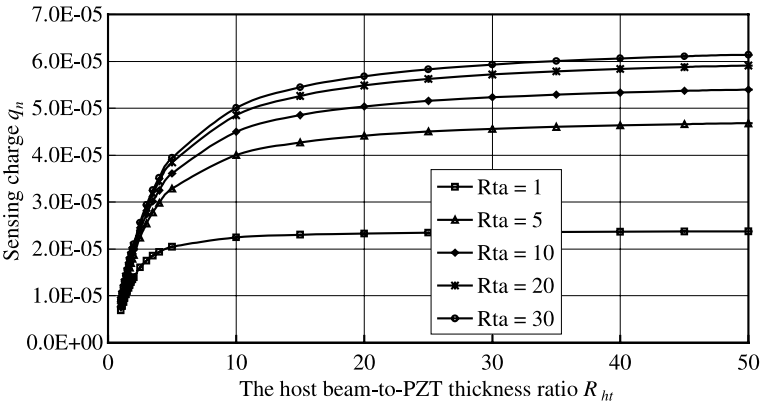


Fig. 14. Sensing charges ($q_n$) caused by the bending moment versus $R_{\mathrm{ht}}$ with $R_{\mathrm{ta}}$ ranging from 1 to 30.

*2.2.2. Sensing charge caused by a bending moment*

When a bending moment ($M_0$) is applied to the host beam at the free end as shown in Fig. 1, we can also choose $M_0$ so that $\varepsilon_m$ is $-7.43$ με. In doing so, Eqs. (46) of Part I become

$$H_{nk} = r_{\mathrm{a}}\varepsilon_m, \quad H_{mk} = \frac{2r_{\mathrm{av}}}{r_{\mathrm{h}}}\varepsilon_m, \quad H_{qk} = 0, \qquad k = \mathrm{I}, \mathrm{II}, \quad \text{where } \varepsilon_m = -7.43\ \mu\varepsilon \tag{3}$$

Using Eq. (3) and the same material and geometric parameters, we can calculate the shear and peel stresses, and then the sensing charge. The distribution patterns of the shear and peel stresses caused by the applied bending moment are similar to those actuated by the applied voltage. The sensing electric charge due to the applied bending moment, also similar to that due to the applied axial force, is plotted versus the thickness ratio $R_{\mathrm{ht}}$ for a range of thickness ratio $R_{\mathrm{ta}}$ in Fig. 14.

## 3. The host beam with two symmetrically bonded PZTs and comparisons

Crawley and de Luis (1987) investigated the active behaviors of the smart beam with two symmetrically bonded PZT patches. The theory of Crawley and de Luis (1987) was based on the assumptions: (a) only extensional deformation is permitted in the PZT patch, (b) only shear stress exists in the adhesive layer, (c) the host beam is deformed in extension or bending. Based on these assumptions, they derived the expressions for the shear stress in the adhesive and the equivalent forces in the host beam as follows:

$$\tau_{n\mathrm{c}} = A_{\mathrm{c}1}\sinh\beta_{\mathrm{c}}\xi, \quad \text{where } A_{\mathrm{c}1} = \frac{H_{n\mathrm{II}} + H_{n\mathrm{I}}}{2\beta_{\mathrm{c}}\cosh\beta_{\mathrm{c}}} \tag{4}$$

$$N_{\mathrm{eqc}} = \frac{2r_{\mathrm{h}}E_{n\mathrm{h}}}{2+\psi}(\varepsilon_e), \quad M_{\mathrm{eqc}} = -\frac{r_{\mathrm{h}}^2E_{n\mathrm{h}}}{6+\psi}(\varepsilon_e) \quad \text{in which } \psi = \frac{r_{\mathrm{h}}E_{n\mathrm{h}}}{r_1E_{n1}} \tag{5}$$

where

$$\beta_{\mathrm{c}} = \sqrt{\frac{R_{\mathrm{ta}}}{r_1^2}\left(\frac{1}{E_{n1}} + \frac{\alpha}{E_{n\mathrm{h}}R_{\mathrm{ht}}}\right)}, \quad \alpha = 2 \text{ for extension, and } \alpha = 6 \text{ for bending.}$$

In the above equations, the present symbols and definitions of the non-dimensional parameters have been used. To compare the performance of the PZT actuators and sensors, we derive the following equations based on Eq. (4).

The non-dimensional axial force and bending moment at $\xi = 0$ are

$$N_{\text{maxc}} = \frac{2A_{\text{c1}}}{\beta_{\text{c}}}(1 - \cosh\beta_{\text{c}}), \qquad M_{\text{maxc}} = \frac{r_{\text{h}}A_{\text{c1}}}{\beta_{\text{c}}}(\cosh\beta_{\text{c}} - 1) \tag{6}$$

The actuated axial displacement is

$$\left.\begin{aligned} u_{n\text{hc}} &= \tfrac{2A_{\text{c1}}}{E_{n\text{h}}r_{\text{h}}\beta_{\text{c}}}\left[\tfrac{1}{\beta_{\text{c}}}(\sinh\beta_{\text{c}}\xi + \sinh\beta_{\text{c}}) - (\xi+1)\cosh\beta_{\text{c}}\right] \\ \Delta l_{n\text{hc}} &= u_{n\text{hc}}(1) - u_{n\text{hc}}(-1) = -\tfrac{4A_{\text{c1}}}{E_{n\text{h}}r_{\text{h}}\beta_{\text{c}}}\left(\cosh\beta_{\text{c}} - \tfrac{1}{\beta_{\text{c}}}\sinh\beta_{\text{c}}\right) \end{aligned}\right\} \tag{7}$$

The actuated deflection is given by

$$\left.\begin{aligned} w_{n\text{hc}} &= J_{\text{c}}(\xi) + \tfrac{\mathrm{d}J_{\text{c}}(1)}{\mathrm{d}\xi}(\xi+1) - J_{\text{c}}(1) \\ w_{n\text{hc}}(1) &= 2\tfrac{\mathrm{d}J_{\text{c}}(1)}{\mathrm{d}\xi} \quad \text{and} \quad \tfrac{\mathrm{d}w_{n\text{hc}}(1)}{\mathrm{d}\xi} = 2\tfrac{\mathrm{d}J_{\text{c}}(1)}{\mathrm{d}\xi} \end{aligned}\right\} \tag{8}$$

in which

$$J_{\text{c}}(\xi) = \frac{12A_{\text{c1}}}{E_{n\text{h}}r_{\text{h}}^2\beta_{\text{c}}}\left(\frac{\xi^2}{2}\cosh\beta_{\text{c}} - \frac{1}{\beta_{\text{c}}^2}\cosh\beta_{\text{c}}\xi\right) \tag{9}$$

The sensing electric charge is

$$q_{n\text{c}} = \frac{2e_{31}A_{\text{c1}}}{E_{n1}r_1\beta_{\text{c}}^2}(\beta_{\text{c}}\cosh\beta_{\text{c}} - \sinh\beta_{\text{c}}) \tag{10}$$

In the above equations, subscript c denotes that they are derived using the shear lag model developed by Crawley and de Luis (1987). The related results for the present model were derived in Part I except for $\Delta l_{n\text{h}}$, which can be easily obtained by integrating the axial force. In the following numerical results, the same data as those used in the case of a host beam with one bonded PZT are employed.

### 3.1. Both PZTs used as actuators

Consider both PZTs are bonded in such a way that they have the same poling direction. When both PZTs are subjected to an electric field of the same magnitude and direction, the host beam is deformed longitudinally. When an electric field of the same value and opposite direction is applied to PZT1 and PZT2, respectively, the host beam is deformed in pure bending. The two cases were investigated by Crawley and de Luis (1987). The distribution patterns of the present shear and peel stresses in the adhesive, and the actuated forces in the host beam are the same as those illustrated in Figs. 3–9, and thus are not given here.

#### 3.1.1. The actuated stresses and comparisons

Figs. 15 and 16 show the influence of thickness ratio $R_{\text{ht}}$ on the present shear and peel stresses of PZT1 at $\xi = 1$ as well as the comparison with the shear stress predicted by Crawley and de Luis (1987). Fig. 15 denotes the edge stresses of PZT1 versus the host beam-to-PZT thickness ratio $R_{\text{ht}}$ when both PZTs are subjected to a voltage of −100 V. In this case, the host beam deforms longitudinally. Fig. 16 indicates the edge stresses when a voltage of 100 V is applied to PZT1 and PZT2 creating opposite electric fields. In this case, the host beam deforms in bending and it can be seen that, when $R_{\text{ht}} > \sqrt{2}$, the peel stress is positive, and the negative peel stress occurs when $R_{\text{ht}} < \sqrt{2}$.

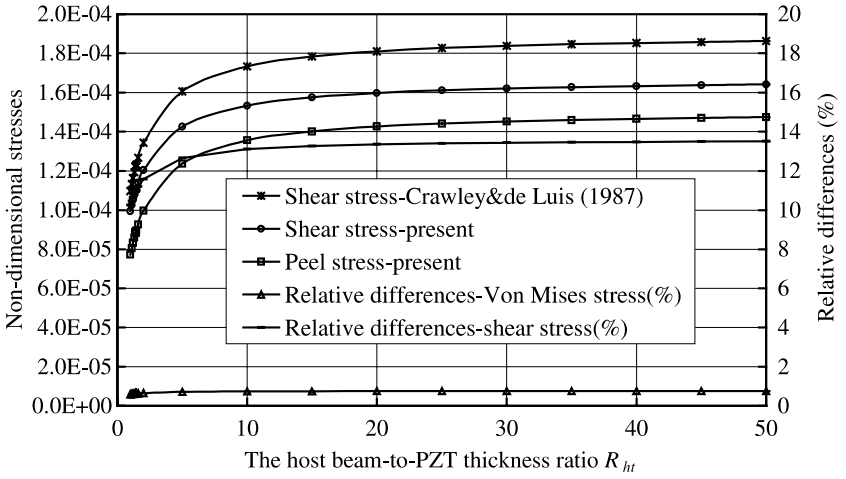


Fig. 15. Non-dimensional stresses for the host beam in extension versus $R_{ht}$ with $R_{ta} = 10$ and comparison with Crawley and de Luis (1987).

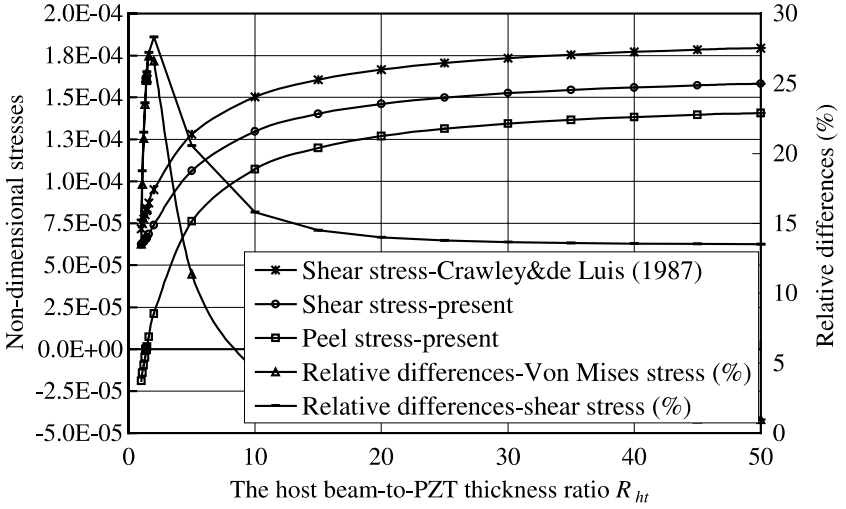


Fig. 16. Non-dimensional stresses for the host beam in bending versus $R_{ht}$ with $R_{ta} = 10$ and comparison with Crawley and de Luis (1987).

It can be seen from Figs. 15 and 16 that, the present shear stress is less than that predicted by Crawley and de Luis (1987). When the host beam deforms in extension, the relative difference is in the range of from 10% to 14%. When the host beam deforms in bending, the difference is larger than 20% for $R_{ht}$ ranging from 1.2 to 2 and larger than 10% in the other ranges of $R_{ht}$.

As the peel stress exists in the present model but not in the shear lag model (Crawley and de Luis, 1987), we may use the Von Mises stress for the comparisons, which is defined by

$$\sigma_{von} = \sqrt{\sigma_n^2 + 3\tau_n^2} \tag{11}$$

The present Von Mises stress is also less than that predicted by the shear lag for both extension and bending. Fig. 15 shows that, when the host beam deforms in extension, the relative difference of the Von Mises stress between the present model and the shear lag model is less than 1%. Nevertheless, as shown in Fig. 16, when the host beam deforms in bending, the difference is larger than 10% when $R_{ht}$ is less than 5, and it is as larger as up to 27% at $R_{ht} = 1.6$.

### 3.1.2. The actuated forces and comparisons

It should be noted that, the equivalent forces shown in Eq. (5) and the maximum forces shown in Eq. (6) derived from the shear stress model developed by Crawley and de Luis (1987) are very close for the thin adhesive layer. It can be shown that, for the used data in this paper, the relative difference is less than 2% when $R_{ta} = 10$, and less than 0.5% when $R_{ta} = 20$. The equivalent forces will be investigated in Section 4, and the present maximum forces $N_{max}$ and those of the shear lag model $N_{maxc}$ are listed in Table 1.

Table 1 shows that the differences of the actuated axial forces between the present model and the shear lag model are less than 0.2%. Because Fig. 15 indicates that the maximum shear stress in the present model is less than that predicted by Crawley and de Luis (1987), the shear stress in the shear lag model is slightly more concentrated in the adhesive end regions. Therefore, the relative difference between the actuated extensional displacements $\Delta l_{nh}$ and those of the shear lag model $\Delta l_{nhc}$ is slightly larger, as shown in Table 2.

Table 2 lists the elongations of a host beam and a comparison with the shear lag model, which shows that the differences of the present elongations and those predicted by the shear lag model are less than 2%.

Tables 1 and 2 show that, when the host beam deforms in extension, the actuated performance predicted by the shear lag model is in a good agreement with that predicted by the present model.

When the host beam deforms in bending, the actuated bending moment at $\xi = 0$ and the deflection at $\xi = 1$ are shown in Figs. 17 and 18. The actuated bending moment shown in Fig. 17 is divided by $R_{ht}$ for better presentation. It can be seen from Fig. 16 that, the peel stress is negative when $E_h R_{ht}^2$ is less than $2E_1$, or $R_{ht} < \sqrt{2}$ for $E_h = E_1$, and it is positive when $R_{ht} > \sqrt{2}$. Therefore, the direction of the bending moment calculated by the peel stress is opposite to that by the shear stress when $R_{ht} < \sqrt{2}$, and the direction of the

Table 1
The actuated axial forces and comparisons

| $R_{ht}$ | $R_{ta} = 10$ | | | $R_{ta} = 20$ | | |
|---|---|---|---|---|---|---|
| | $-N_{maxc}$ | $-N_{max}$ | Error (%) | $-N_{maxc}$ | $-N_{max}$ | Error (%) |
| 1 | 3.23E−05 | 3.23E−05 | 4.55E−03 | 3.24E−05 | 3.24E−05 | 6.93E−02 |
| 1.1 | 3.44E−05 | 3.44E−05 | 3.16E−03 | 3.45E−05 | 3.45E−05 | 3.19E−03 |
| 1.2 | 3.63E−05 | 3.63E−05 | 1.45E−03 | 3.64E−05 | 3.64E−05 | 3.58E−03 |
| 1.3 | 3.81E−05 | 3.81E−05 | 5.16E−04 | 3.83E−05 | 3.83E−05 | 3.91E−03 |
| 1.4 | 3.98E−05 | 3.98E−05 | 2.67E−03 | 4.00E−05 | 4.00E−05 | 4.19E−03 |
| 1.41 | 4.00E−05 | 4.00E−05 | 2.90E−03 | 4.02E−05 | 4.02E−05 | 4.21E−03 |
| 1.42 | 4.02E−05 | 4.02E−05 | 3.12E−03 | 4.03E−05 | 4.03E−05 | 4.23E−03 |
| 1.45 | 4.07E−05 | 4.07E−05 | 3.80E−03 | 4.08E−05 | 4.08E−05 | 4.30E−03 |
| 1.6 | 4.30E−05 | 4.29E−05 | 7.37E−03 | 4.32E−05 | 4.32E−05 | 4.57E−03 |
| 2 | 4.82E−05 | 4.82E−05 | 1.74E−02 | 4.86E−05 | 4.86E−05 | 4.78E−03 |
| 5 | 6.81E−05 | 6.80E−05 | 7.46E−02 | 6.92E−05 | 6.92E−05 | 1.55E−03 |
| 10 | 7.88E−05 | 7.87E−05 | 1.15E−01 | 8.06E−05 | 8.06E−05 | 1.04E−02 |
| 15 | 8.31E−05 | 8.30E−05 | 1.32E−01 | 8.53E−05 | 8.53E−05 | 1.51E−02 |
| 20 | 8.54E−05 | 8.53E−05 | 1.42E−01 | 8.78E−05 | 8.78E−05 | 1.79E−02 |
| 25 | 8.69E−05 | 8.68E−05 | 1.48E−01 | 8.94E−05 | 8.94E−05 | 1.97E−02 |
| 30 | 8.79E−05 | 8.78E−05 | 1.52E−01 | 9.05E−05 | 9.05E−05 | 2.10E−02 |
| 35 | 8.86E−05 | 8.85E−05 | 1.56E−01 | 9.13E−05 | 9.13E−05 | 2.20E−02 |
| 40 | 8.92E−05 | 8.91E−05 | 1.58E−01 | 9.19E−05 | 9.19E−05 | 2.28E−02 |
| 50 | 9.00E−05 | 8.98E−05 | 1.61E−01 | 9.28E−05 | 9.28E−05 | 2.39E−02 |

Table 2
The extensional displacements and comparisons

| $R_{ht}$ | $R_{ta} = 10$ | | | $R_{ta} = 20$ | | |
|---|---|---|---|---|---|---|
| | $-\Delta l_{nhc}$ | $-\Delta l_{nh}$ | Error (%) | $-\Delta l_{nhc}$ | $-\Delta l_{nh}$ | Error (%) |
| 1 | 8.44E−06 | 8.34E−06 | 1.22E+00 | 8.87E−06 | 8.76E−06 | 1.26E+00 |
| 1.1 | 8.12E−06 | 8.02E−06 | 1.25E+00 | 8.55E−06 | 8.45E−06 | 1.25E+00 |
| 1.2 | 7.83E−06 | 7.73E−06 | 1.27E+00 | 8.26E−06 | 8.15E−06 | 1.27E+00 |
| 1.3 | 7.56E−06 | 7.46E−06 | 1.29E+00 | 7.98E−06 | 7.88E−06 | 1.29E+00 |
| 1.4 | 7.31E−06 | 7.21E−06 | 1.31E+00 | 7.73E−06 | 7.63E−06 | 1.31E+00 |
| 1.41 | 7.28E−06 | 7.19E−06 | 1.31E+00 | 7.70E−06 | 7.60E−06 | 1.31E+00 |
| 1.42 | 7.26E−06 | 7.16E−06 | 1.31E+00 | 7.68E−06 | 7.58E−06 | 1.31E+00 |
| 1.45 | 7.18E−06 | 7.09E−06 | 1.32E+00 | 7.60E−06 | 7.50E−06 | 1.32E+00 |
| 1.6 | 6.85E−06 | 6.76E−06 | 1.34E+00 | 7.26E−06 | 7.16E−06 | 1.34E+00 |
| 2 | 6.09E−06 | 6.00E−06 | 1.39E+00 | 6.48E−06 | 6.39E−06 | 1.39E+00 |
| 5 | 3.33E−06 | 3.28E−06 | 1.56E+00 | 3.60E−06 | 3.54E−06 | 1.55E+00 |
| 10 | 1.90E−06 | 1.87E−06 | 1.63E+00 | 2.07E−06 | 2.03E−06 | 1.62E+00 |
| 15 | 1.33E−06 | 1.31E−06 | 1.66E+00 | 1.45E−06 | 1.43E−06 | 1.64E+00 |
| 20 | 1.02E−06 | 1.00E−06 | 1.68E+00 | 1.12E−06 | 1.10E−06 | 1.66E+00 |
| 25 | 8.30E−07 | 8.16E−07 | 1.69E+00 | 9.09E−07 | 8.94E−07 | 1.67E+00 |
| 30 | 6.99E−07 | 6.87E−07 | 1.69E+00 | 7.66E−07 | 7.53E−07 | 1.67E+00 |
| 35 | 6.03E−07 | 5.93E−07 | 1.70E+00 | 6.62E−07 | 6.51E−07 | 1.68E+00 |
| 40 | 5.31E−07 | 5.22E−07 | 1.70E+00 | 5.83E−07 | 5.73E−07 | 1.68E+00 |
| 50 | 4.28E−07 | 4.21E−07 | 1.71E+00 | 4.70E−07 | 4.62E−07 | 1.68E+00 |

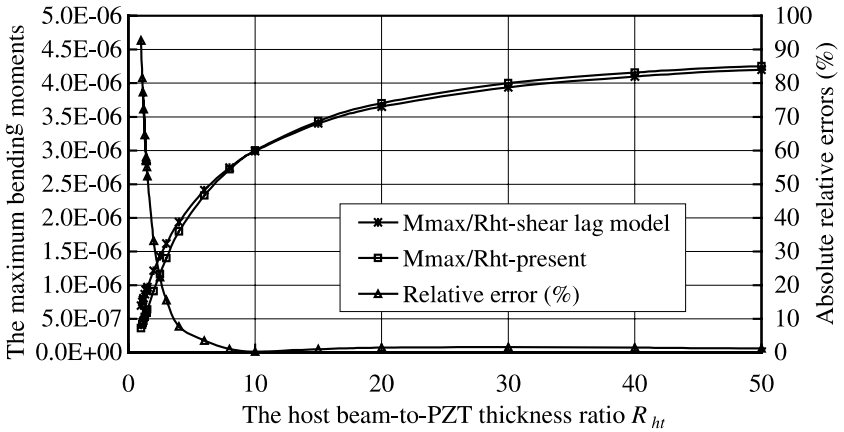


Fig. 17. The maximum bending moment of the non-dimensional form versus $R_{ht}$ with $R_{ta} = 10$ and comparison with the shear lag model.

bending moment due to the peel stress is the same as that by the shear stress when $R_{ht} > \sqrt{2}$. Because of this peel stress effect, the present bending moment at $\xi = 0$ is less than that predicted by the shear lag model when $R_{ht} < 10$, and larger than that of the shear stress model when $R_{ht} > 10$, as shown in Fig. 17. When the host beam-to-PZT thickness ratio $R_{ht}$ is larger than 10, the maximum bending moment predicted by the shear lag model is 1% less than that predicted by the present model. However, when $R_{ht}$ is equal to 4, 3, 2, 1.5 and 1, the present bending moment is 7.76%, 15.6%, 33.3%, 52.4% and 92.7% lower than those predicted by the shear lag model, respectively.

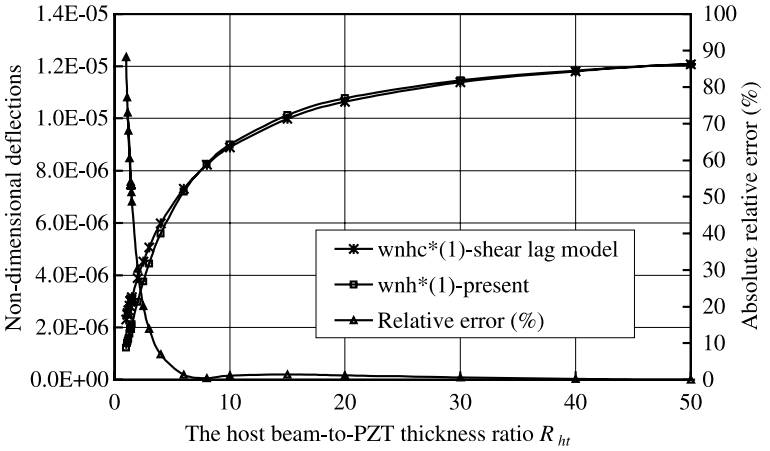


Fig. 18. Non-dimensional deflection at $\xi = 1$ versus $R_{\mathrm{ht}}$ with $R_{\mathrm{ta}} = 10$ and comparison with the shear lag model.

The present deflection of the host beam and that of the shear lag model are determined by Eq. (42) of Part I and Eq. (8), respectively. At $\xi = 1$, the non-dimensional deflection is equal to the non-dimensional rotational angle of the cross-section so that we only need to compare the deflection at $\xi = 1$, or compare $w_{n\mathrm{h}}(1)$ with $w_{n\mathrm{hc}}(1)$. In order to demonstrate differences clearly, we plot Fig. 18 whose three curves represent $w^*_{n\mathrm{h}}(1) \sim R_{\mathrm{ht}}$, $w^*_{n\mathrm{hc}}(1) \sim R_{\mathrm{ht}}$ and the absolute relative error versus $R_{\mathrm{ht}}$, in which

$$w^*_{n\mathrm{h}}(1) = -R_{\mathrm{ht}} w_{n\mathrm{h}}(1), \quad w^*_{n\mathrm{hc}}(1) = -R_{\mathrm{ht}} w_{n\mathrm{hc}}(1), \quad \text{and the relative error} = \frac{|w_{n\mathrm{h}}(1) - w_{n\mathrm{hc}}(1)|}{|w_{n\mathrm{h}}(1)|} \times 100$$

The deflection difference between the present model and the shear lag model is less than 2% when the host beam-to-PZT thickness ratio $R_{\mathrm{ht}}$ is larger than 10. Nevertheless, the magnitude of the deflection at $\xi = 1$ predicted by the shear lag model is 6.92%, 13.9%, 30.4%, 48.7% and 88.2% higher than that of the present model when $R_{\mathrm{ht}}$ is equal to 4, 3, 2, 1.5 and 1. Therefore, the shear lag model may not be applied to the flexible structures deformed in bending, especially when $R_{\mathrm{ht}} \leqslant 3$ for the selected data.

### 3.2. Both PZTs used as sensors

If an axial force is applied to the host beam, it deforms longitudinally and the same electric charges will be sensed in PZT1 and PZT2. In this case, employing the same data used before, we give the sensing charges caused by the axial force and comparisons with the shear lag model shown in Fig. 19. It can be seen that, the present charges are always less than those predicted by the shear lag model and the differences are only within 1–2%.

When a bending moment is applied to the host beam shown in Fig. 2, it deforms in bending. In this case, the electric charges with the same value but opposite will be sensed in two PZT patches, respectively. Fig. 20 shows the sensing charges $q_n$ versus the host beam-to-PZT patch thickness ratio $R_{\mathrm{ht}}$ with $R_{\mathrm{ta}} = 10$ and the comparison with the shear lag model. In Fig. 20, the constant strain $\varepsilon_m (= \pm 7.43\ \mu\varepsilon)$ caused by the bending moment is assumed, which means that the bending moment applied to the host beam varies with its thickness.

Fig. 20 shows that, the present charge caused by the bending moment is larger than that predicted by the shear lag mode when $R_{\mathrm{ht}} > 8$, and their difference is less than 1%. However, when $R_{\mathrm{ht}}$ is equal to 4, 3, 2, 1.5 and 1, the present charge is 6.92%, 13.9%, 30.4%, 48.7% and 88.2% lower than that predicted by the shear

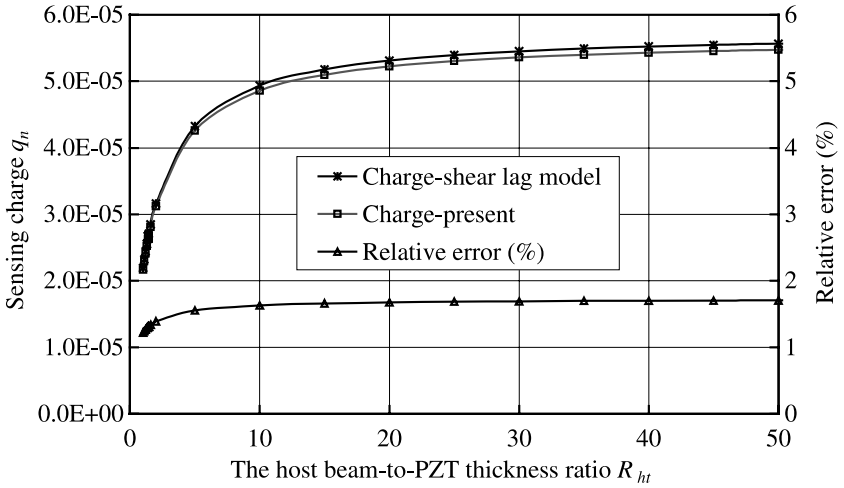


Fig. 19. Sensing charges ($q_n$) caused by the axial force versus $R_{\mathrm{ht}}$ with $R_{\mathrm{ta}} = 10$ and comparison with the shear lag model.

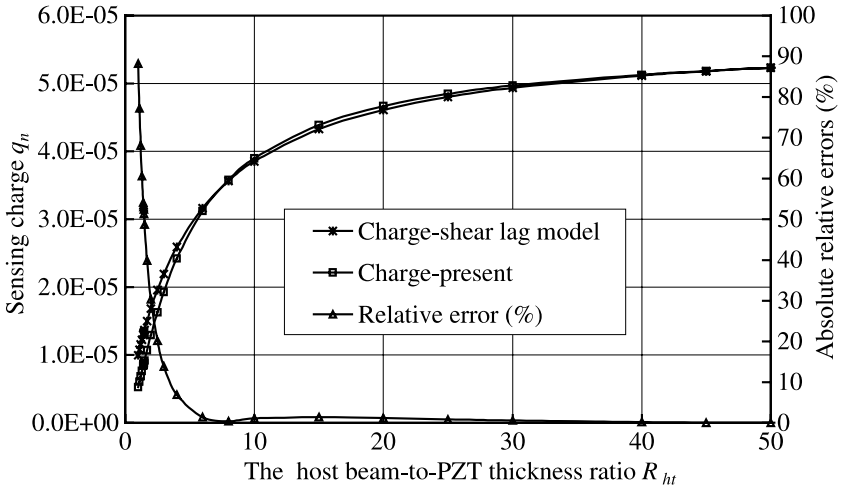


Fig. 20. Sensing charges ($q_n$) caused by the bending moment versus $R_{\mathrm{ht}}$ with $R_{\mathrm{ta}} = 10$ and comparison with the shear lag model.

lag model, respectively. We can show that, when $R_{\mathrm{ht}}$ tends to 1, the peel stress increases with the reducing $R_{\mathrm{ht}}$, and the shear stress decreases in this case; therefore, the peel stress affects the sensing charge greatly in this case.

## 4. Verification, comparison and discussion

### *4.1. Comparison with the shooting method*

The coupled differential equations can be solved using numerical methods. Tong et al. (2001) have solved the governing equations using the multi-segment shooting method. To verify the present exact solutions, we compare the present numerical results with those obtained by the shooting method. Tables 3 and 4

Table 3
The comparisons of the actuated performance with the shooting method

| $R_{ta}$ | $R_{ht}$ | The actuated axial force ($-N_{nh}$) | | The actuated bending moment ($M_{nh}$) | |
|---|---|---|---|---|---|
| | | Present solution | Shooting method | Present solution | Shooting method |
| 10 | 1 | 3.23260E−05 | 3.23260E−05 | 3.59980E−07 | 3.59981E−07 |
| | 2 | 4.82037E−05 | 4.82039E−05 | 1.82226E−06 | 1.82226E−06 |
| | 3 | 5.75449E−05 | 5.75447E−05 | 4.19654E−06 | 4.19654E−06 |
| | 4 | 6.36804E−05 | 6.36804E−05 | 7.18790E−06 | 7.18790E−06 |
| | 5 | 6.80154E−05 | 6.80154E−05 | 1.05923E−05 | 1.05923E−05 |
| 20 | 1 | 3.23951E−05 | 3.23952E−05 | 3.59986E−07 | 3.59986E−07 |
| | 2 | 4.85612E−05 | 4.85614E−05 | 1.82243E−06 | 1.82243E−06 |
| | 3 | 5.82271E−05 | 5.82271E−05 | 4.19881E−06 | 4.19881E−06 |
| | 4 | 6.46495E−05 | 6.46496E−05 | 7.19907E−06 | 7.19919E−06 |
| | 5 | 6.92248E−05 | 6.92247E−05 | 1.06243E−05 | 1.06243E−05 |

Table 4
The comparisons of the sensing charge with the shooting method

| $R_{ta}$ | $R_{ht}$ | The sensing charge $q_n$ caused by $N$ | | The sensing charge $q_n$ caused by $M$ | |
|---|---|---|---|---|---|
| | | Present solution | Shooting method | Present solution | Shooting method |
| 10 | 1 | 2.16849E−05 | 2.16851E−05 | 5.29753E−06 | 5.29830E−06 |
| | 2 | 3.12081E−05 | 3.12085E−05 | 1.29220E−05 | 1.29234E−05 |
| | 3 | 3.66315E−05 | 3.66319E−05 | 1.92706E−05 | 1.92797E−05 |
| | 4 | 4.01389E−05 | 4.01394E−05 | 2.42279E−05 | 2.42476E−05 |
| | 5 | 4.25945E−05 | 4.25950E−05 | 2.81100E−05 | 2.81409E−05 |
| 20 | 1 | 2.28134E−05 | 2.27854E−05 | 5.43657E−06 | 5.43737E−06 |
| | 2 | 3.32868E−05 | 3.32262E−05 | 1.33541E−05 | 1.33556E−05 |
| | 3 | 3.93682E−05 | 3.92829E−05 | 2.00744E−05 | 2.00841E−05 |
| | 4 | 4.33472E−05 | 4.32433E−05 | 2.54078E−05 | 2.54291E−05 |
| | 5 | 4.61546E−05 | 4.60364E−05 | 2.96388E−05 | 2.96725E−05 |

list the actuated stress resultants and the sensing charges for the host beam with two symmetrically bonded PZT patches and compare those predicted using the shooting method. Because the difference between the present model including the peel stress and the shear lag model mainly exists in the flexible structures, Tables 3 and 4 only give the results for the flexible structures, for which the thickness ratio $R_{ht}$ is small.

Tables 3 and 4 reveal that there exists an excellent agreement between the present exact solutions and those predicted using the shooting method for the actuated force and bending moment at $\xi = 0$, and the sensing charges caused by an axial force and a bending moment.

### 4.2. The actuated equivalent stress resultants

The main difference between the present model and the shear lag model lies in peel stress and the PZT model. Crawley and de Luis (1987) derived the equivalent forces based on the PZT rod model, which was also employed by Wang and Rogers (1991). In the present work, the PZT patch is modelled as a beam. Using the PZT beam model, we also derive the equivalent stress resultant based on the same principles and the linear strain distribution assumptions as those by Crawley and de Luis (1987).

The equilibrium conditions for the host beam with one PZT are

$$\left.\begin{aligned}&(E_1A_1+E_2A_h)\frac{du}{dx}-(E_1S_{1y}+E_hS_{hy})\frac{d^2w}{dx^2}+\frac{A_1e_{31}}{t_1}V_1=0\\&(E_1S_{1y}+E_hS_{hy})\frac{du}{dx}-(E_1I_{1y}+E_hI_{hy})\frac{d^2w}{dx^2}+\frac{S_{1y}e_{31}}{t_1}V_1=0\end{aligned}\right\}\tag{12}$$

The equilibrium conditions for the host beam with two symmetrically bonded PZTs are

$$\left.\begin{aligned}&(E_1A_1+E_hA_h+E_2A_2)\frac{du}{dx}-(E_1S_{1y}+E_hS_{hy}+E_2S_{2y})\frac{d^2w}{dx^2}+\frac{A_1(e_{31})_1}{t_1}V_1+\frac{A_2(e_{31})_2}{t_2}V_2=0\\&(E_1S_{1y}+E_hS_{hy}+E_2S_{2y})\frac{du}{dx}-(E_1I_{1y}+E_hI_{hy}+E_2I_{2y})\frac{d^2w}{dx^2}+\frac{S_{1y}(e_{31})_1}{t_1}V_1+\frac{S_{2y}(e_{31})_2}{t_2}V_2=0\end{aligned}\right\}\tag{13}$$

In Eqs. (12) and (13), subscripts 1, 2 and h represent PZT1, PZT2 and the host beam; $E_k$, $A_k$, $S_{ky}$, and $I_{ky}$ $(k=1,2,\mathrm{h})$ are the elastic moduli, cross-section areas, area and inertia moments, and $y$ is the neutral axis referring to cross-section of the whole composite beam.

By using the non-dimensional definitions and the constitutive relations of the host beam given in Part I, Eqs. (12) and (13) can be rewritten as

The host beam with one PZT patch:

$$\left.\begin{aligned}&(1+\psi)N_{eq}-\tfrac{12r_{ht}}{r_h^2}M_{eq}=r_hE_{nh}(\varepsilon_e)\\&(r_{tc}-r_{hc}\psi)N_{eq}-\left[\psi+\tfrac{1}{r_h^2}(r_1^2+12r_{tc}r_{ht})\right]M_{eq}=r_hE_{nh}r_{tc}(\varepsilon_e)\end{aligned}\right\}\tag{14}$$

The host beam with two PZT patches:

$$\left.\begin{aligned}&(2+\psi)N_{eq}=2r_hE_{nh}(\varepsilon_e)\\&\left[\psi+\tfrac{2}{r_h^2}(r_1^2+12r_{ht}^2)\right]M_{eq}=-2r_hE_{nh}r_{tc}(\varepsilon_e)\end{aligned}\right\}\tag{15}$$

where

$$r_{hc}=\frac{h_c}{L},\quad r_{tc}=\frac{t_c}{L},\quad r_{ht}=\frac{1}{2}(r_h+r_1)$$

in which $N_{eq}$ and $M_{eq}$ are the non-dimensional axial force and bending moment; $h_c$ and $t_c$ are the distance from the neutral axis of the host beam and the PZT patch to that of the whole composite beam, respectively, it is also assumed that the adhesive is very thin like the shear lag model and its thickness is neglected.

Solutions of Eqs. (14) and (15) are given by

The host beam with one PZT patch:

$$\left.\begin{aligned}N_{eq}&=\frac{E_{nh}r_h\left(1+\frac{1}{\psi R_{ht}^2}\right)}{4\left(1+\frac{3}{2R_{ht}}+\frac{1}{R_{ht}^2}\right)+\psi\left(1+\frac{1}{\psi^2R_{ht}^2}\right)}(\varepsilon_e)\\M_{eq}&=-\frac{E_{nh}r_h^2\left(1+\frac{1}{R_{ht}}\right)}{2\left[4\left(1+\frac{3}{2R_{ht}}+\frac{1}{R_{ht}^2}\right)+\psi\left(1+\frac{1}{\psi^2R_{ht}^2}\right)\right]}(\varepsilon_e)\end{aligned}\right\}\tag{16}$$

The host beam with two PZT patches:

$$N_{eq}=\frac{2r_hE_{nh}}{2+\psi}(\varepsilon_e),\qquad M_{eq}=-\frac{E_{nh}r_h^2\left(1+\frac{1}{R_{ht}}\right)}{2\left[3\left(1+\frac{1}{R_{ht}}\right)^2+\left(\frac{1}{R_{ht}}\right)^2\right]+\psi}(\varepsilon_e)\tag{17}$$

It is found that the equivalent axial force shown in Eq. (17) is the same as that derived by Crawley and de Luis (1987). It is evident that, with the increase of $R_{ht}$, the present equivalent bending moment approaches to that formulated by Crawley and de Luis (1987). When the host beam-to-PZT thickness ratio $R_{ht}$ is much

larger than 1, or the thickness of the host beam is much larger than that of the PZT patch, present Eq. (17) reduces to Eq. (5). Nevertheless, when the PZT actuators are used in the flexible structures, the difference of the equivalent bending moment between two models is significant, which is similar to the large difference of the maximum bending moment.

Table 5 gives the comparisons between the present equivalent bending moment shown in Eq. (17) and the maximum values calculated by the exact solution for the case of a host beam with two symmetrically bonded two PZTs.

In Table 5, $M_{\max}$ $(R_{\mathrm{ta}} = 10)$ is the maximum bending moment for $R_{\mathrm{ta}} = 10$, $M_{\max}$ $(R_{\mathrm{ta}} = 20)$ is the maximum bending moment for $R_{\mathrm{ta}} = 20$ and $M_{\mathrm{eq}}$ is the equivalent bending moment; Error (1) and Error (2) are defined by

$$\mathrm{Error}(1) = \frac{|M_{\mathrm{eq}} - M_{\max}(R_{\mathrm{ta}} = 10)|}{M_{\mathrm{eq}}} \times 100, \qquad \mathrm{Error}(2) = \frac{|M_{\mathrm{eq}} - M_{\max}(R_{\mathrm{ta}} = 20)|}{M_{\mathrm{eq}}} \times 100 \tag{18}$$

Table 5 shows that, the equivalent bending moment given by (17) is in good agreement with the maximum value given by the exact solution for the thin adhesive. The equivalent axial force given by Eq. (17), being equal to that given by Crawley and de Luis (1987), is also an excellent approximation.

For the equivalent forces of the host beam with one PZT patch, given by Eq. (16), similar numerical results can be obtained. It can be shown that they are good approximation to the maximum axial force and bending moment. When the PZT-to-adhesive layer thickness ratio $R_{\mathrm{ta}}$ is equal to 10, the relative differences of the equivalent and maximum values are less than 0.8% for the host beam-to-PZT thickness ratio $R_{\mathrm{ht}}$ ranging from 1 to 5, less than 2% for $R_{\mathrm{ht}} \leqslant 10$ and less than 4% for $R_{\mathrm{ht}} \leqslant 100$. When the PZT-to-adhesive

Table 5
The present maximum and equivalent bending moments and comparisons

| $R_{\mathrm{ht}}$ | $M_{\max}$ $(R_{\mathrm{ta}} = 10)$ | $M_{\max}$ $(R_{\mathrm{ta}} = 20)$ | $M_{\mathrm{eq}}$ | Error (1) (%) | Error (2) (%) |
|---|---|---|---|---|---|
| 1 | 3.60E−07 | 3.60E−07 | 3.60E−07 | 1.56E−03 | 1.62E−05 |
| 1.2 | 5.64E−07 | 5.64E−07 | 5.64E−07 | 1.83E−03 | 1.42E−05 |
| 1.4 | 8.14E−07 | 8.14E−07 | 8.14E−07 | 2.60E−03 | 2.38E−05 |
| 1.41 | 8.28E−07 | 8.28E−07 | 8.28E−07 | 2.65E−03 | 2.50E−05 |
| 1.42 | 8.42E−07 | 8.42E−07 | 8.42E−07 | 2.70E−03 | 2.63E−05 |
| 1.46 | 8.98E−07 | 8.98E−07 | 8.98E−07 | 2.91E−03 | 3.20E−05 |
| 1.5 | 9.56E−07 | 9.56E−07 | 9.56E−07 | 3.15E−03 | 3.89E−05 |
| 2 | 1.82E−06 | 1.82E−06 | 1.82E−06 | 9.17E−03 | 1.79E−04 |
| 3 | 4.20E−06 | 4.20E−06 | 4.20E−06 | 5.57E−02 | 1.55E−03 |
| 3.6 | 5.93E−06 | 5.94E−06 | 5.94E−06 | 1.14E−01 | 4.32E−03 |
| 3.8 | 6.55E−06 | 6.56E−06 | 6.56E−06 | 1.38E−01 | 5.71E−03 |
| 4 | 7.19E−06 | 7.20E−06 | 7.20E−06 | 1.64E−01 | 7.37E−03 |
| 4.5 | 8.85E−06 | 8.87E−06 | 8.87E−06 | 2.38E−01 | 1.27E−02 |
| 5 | 1.06E−05 | 1.06E−05 | 1.06E−05 | 3.21E−01 | 1.96E−02 |
| 6 | 1.43E−05 | 1.43E−05 | 1.44E−05 | 5.03E−01 | 3.78E−02 |
| 7 | 1.82E−05 | 1.83E−05 | 1.83E−05 | 6.90E−01 | 6.01E−02 |
| 8 | 2.22E−05 | 2.24E−05 | 2.24E−05 | 8.74E−01 | 8.48E−02 |
| 9 | 2.63E−05 | 2.66E−05 | 2.66E−05 | 1.05E+00 | 1.11E−01 |
| 10 | 3.06E−05 | 3.09E−05 | 3.09E−05 | 1.21E+00 | 1.37E−01 |
| 15 | 5.24E−05 | 5.33E−05 | 5.34E−05 | 1.85E+00 | 2.54E−01 |
| 20 | 7.49E−05 | 7.64E−05 | 7.67E−05 | 2.28E+00 | 3.43E−01 |
| 25 | 9.77E−05 | 9.99E−05 | 1.00E−04 | 2.58E+00 | 4.11E−01 |
| 30 | 1.21E−04 | 1.24E−04 | 1.24E−04 | 2.80E+00 | 4.62E−01 |
| 40 | 1.67E−04 | 1.71E−04 | 1.72E−04 | 3.10E+00 | 5.35E−01 |
| 50 | 2.13E−04 | 2.19E−04 | 2.20E−04 | 3.29E+00 | 5.83E−01 |
| 100 | 4.45E−04c | 4.59E−04 | 4.63E−04 | 3.71E+00 | 6.93E−01 |

layer thickness ratio $R_{ta}$ is equal to 20, the differences between the equivalent forces shown in Eq. (16) and the analytical maximum forces are less than 0.07% when the host beam-to-PZT thickness ratio $R_{ht}$ is less than 5, and they are less than 0.8% when $R_{ht}$ is less than 100.

Wang and Rogers (1991) proposed the expressions for the equivalent axial force and bending moment, which can be expressed in terms of the present non-dimensional symbols and definitions as follows:

$$N_{eq} = \frac{r_h E_{nh}}{6+\psi}(\varepsilon_e), \qquad M_{eq} = -\frac{r_h^2 E_{nh}}{2(6+\psi)}(\varepsilon_e) \tag{19}$$

It is noted that, the present definition of the bending moment direction is opposite to that defined by Wang and Rogers (1991).

Comparison of Eqs. (16) with (19) unveils that Eq. (16) does not degenerate to Eq. (19) when the host beam-to-PZT thickness ratio $R_{ht}$ becomes very large. This is different from the comparison of Eqs. (17) and (5). To study the difference for the given data, Figs. 21 and 22 illustrate the non-dimensional equivalent axial force and bending moment versus the host beam-to-PZT patch thickness ratio $R_{ht}$ ranging from 1 to 50, respectively. In Fig. 22, the equivalent bending moment was divided by the thickness ratio $R_{ht}$ for showing the difference clearly.

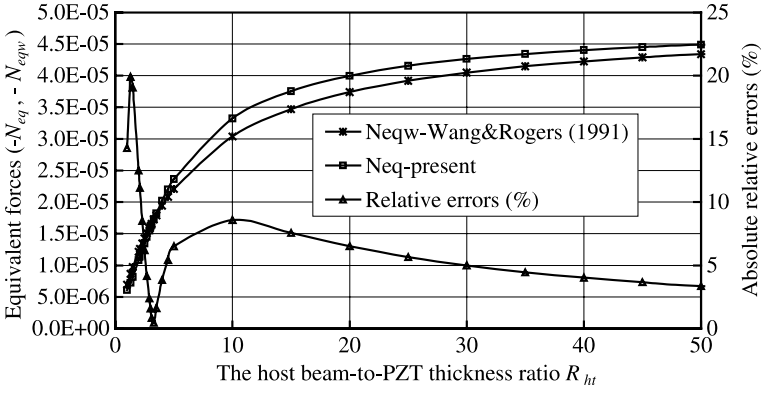


Fig. 21. The equivalent axial force actuated by the applied voltage versus $R_{ht}$ and comparison with Wang and Rogers (1991).

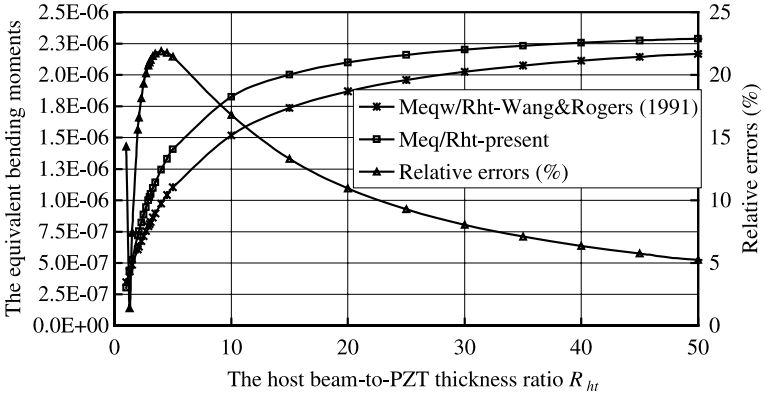


Fig. 22. The actuated-equivalently bending moment divided by $R_{ht}$ versus $R_{ht}$ and comparison with Wang and Rogers (1991).

As shown in Fig. 21, the present equivalent axial force is less than that predicted by Wang and Rogers (1991) when the thickness ratio $R_{ht}$ is less than 3.3, and larger than that using Eq. (19) when $R_{ht} > 3.3$. When thickness ratio $R_{ht}$ is set to 1, 1.3, 3, 5, 10 and 20, the relative difference between the present equivalent axial force and that of Wang and Rogers is −14.3%, −19.9%, −1.6%, 6.5%, 8.6% and 6.5%, respectively. This means that the relative difference between the equivalent forces predicted using Eq. (19) and those predicted using Eq. (16) could be as high as up to 20% for very flexible smart beams. When $R_{ht}$ is set to 30, 40, 50 and 100, the corresponding relative difference is 5%, 4%, 3.4% and 1.8%. This indicates that the relative difference is less than 5% when $R_{ht}$ is greater than 30.

The variation trends of the equivalent bending moments predicted by Eqs. (19) and (16) are similar to those of the equivalent axial force. When $R_{ht}$ is set to 1, 2, 5, 10 and 20, the relative difference is −14.3%, 15.6%, 21.5%, 16.8% and 10.9%, respectively. The relative difference is negative when $R_{ht}$ is less than 1.4, and it becomes positive and increases dramatically when $R_{ht}$ is large than 1.4, and attains its peak when $R_{ht}$ is approximately equal to 4. It is found that the relative difference is over 20% when the thickness ratio $R_{ht}$ ranges approximately between 2.7 and 5. When $R_{ht}$ takes values of 25, 30, 40, 50 and 100, the relative difference is 9.3%, 8%, 7.1%, 5.2% and 2.8%, respectively.

The equivalent axial force and bending moment can be used to calculate the longitudinal deformation and the transverse deflection of the cantilever host beam. The relative differences between the displacements calculated utilizing Eqs. (19) and (16) are found to be similar to those of the equivalent forces and bending moments. They are not given here due to space limitation.

### 4.3. Limitations of the present model and the shear lag model

Goland and Reissner's theory (1944) assumed that the elastic modulus and the thickness of the adhesive were much less than those of the adherents for the flexible joint. The theory developed by Crawley and de Luis (1987) required the same is true in the very thin adhesive layer. The present exact solutions are based on the classic adhesive model presented by Goland and Reissner (1944); therefore, the present theory is also applicable only to the relative thin adhesive with small elastic modulus. Otherwise, a two-dimensional model must be set up. For the selected materials of the PZT patches and the adhesive layer, the PZT patch-to-adhesive thickness ratio $R_{ta}$ should be larger than 10, or even larger than 20.

In light of the demonstrated numerical results, we can draw that, (a) when the host beam deforms in extension, performance of the PZT actuators and sensors predicted by the shear lag model gives the sufficient accuracy; (b) when the host beam deforms in bending, the PZT performance predicted by the shear lag model are correct only if $E_{n\mathrm{h}} r_{\mathrm{h}} \gg E_{n1} r_1$, and if this condition is not satisfied, or for the flexible structures, the peel stress must be included in the smart beam model.

### 4.4. Effect of the material properties

In the demonstrated numerical results, the material properties of the host beam ($E_{\mathrm{h}}$), PZT patches ($E_1$) and adhesive ($E_{\mathrm{a}}$ and $G_{\mathrm{a}}$) are fixed and their relevant thickness vary, which is described by the host beam-to-PZT patch thickness ratio $R_{ht}$ and the PZT-to-adhesive thickness ratio $R_{ta}$. Nevertheless, the influences of the thickness ratios are related to the elastic moduli of the materials. The thickness ratio $R_{ht}$ is related to $E_{\mathrm{h}}$ versus $E_1$ and $R_{ta}$ to $E_1$ versus $E_{\mathrm{a}}$ or $G_{\mathrm{a}}$. To investigate the influences of the material properties, we may also consider the fixed value of the PZT elastic modulus $E_1$.

In light of the constitutive relations of the adhesive, the shear and peel stresses are directly proportional to the ratio $E_{\mathrm{a}}/t_{\mathrm{a}}$ (or $G_{\mathrm{a}}/t_{\mathrm{a}}$). As long as this ratio is constant, the obtained results will be the same. For instance, when the adhesive material with the smaller elastic modulus $E_{\mathrm{a}}$ of $1.5 \times 10^9$ N/m$^2$ is used instead of $3 \times 10^9$ N/m$^2$, the adhesive with thickness 0.05 mm instead of 0.1 mm or $R_{ta} = 20$ will give the same results for the adhesive with $R_{ta} = 10$. Also, the larger elastic modulus of the adhesive requires the thicker

adhesive layer. From the viewpoint of physics, a rigid and relatively thick adhesive layer will behave like a spring in the same way as a soft and relatively thin adhesive layer.

The influence of the host beam-to-PZT elastic module ratio $E_h/E_1$ may be analyzed by considering the equivalent stress resultants shown in Eqs. (16) and (17). Eq. (17) shows that the influence of $E_{nh}/E_{n1}$ on the extension is similar to that of $R_{ht}$, or they can be combined into one item $\psi$ to investigate the PZT performance. However, Eqs. (16) and (17) indicate that the influence of $E_{nh}/E_{n1}$ on bending or the host beam with one PZT patch is much less than that of $R_{ht}$.

## 5. The shear force effect and the edge debonding

In this section, we only consider the case of a host beam with one bonded PZT patch because for the case of a host beam with two symmetrically bonded PZTs, similar results can be obtained.

### 5.1. The shear force effect

When the host beam is subjected to a shear force as shown in Fig. 1, we may also let $\varepsilon_q$ be $-7.63\,\mu\varepsilon$ and thus Eq. (47) of Part I is reduced:

$$H_{n\mathrm{II}} = 0,\ H_{n\mathrm{I}} = r_a\varepsilon_q, \quad H_{m\mathrm{II}} = 0,\ H_{m\mathrm{I}} = \frac{2r_{av}}{r_h}\varepsilon_q, \quad H_{q\mathrm{II}} = H_{q\mathrm{I}} = -\frac{2r_{av}}{r_h}\varepsilon_q \tag{20}$$

in which, we have assumed that $\alpha_L$ is equal to 1. It is assumed that the shear force is applied at $\xi = 1$.

Substituting Eq. (20) and the other data listed in the introduction into the equations given in Appendix A of Part I, we find that all integration constants $A_1$–$A_7$ and $B_1$–$B_6$ are not equal to zero. In this case, the stresses can be expressed as consisting of a symmetric and an anti-symmetric component. The anti-symmetric component of the shear stress and the symmetric component of the peel stress, same as those caused by the bending moment, are similar to those shown in Figs. 3–6. The sensing electric charges, caused by these stress components, are also the same as those caused by the bending moment. The symmetric shear stress and the anti-symmetric peel stress are new and plotted in Figs. 23 and 24. Both figures show that these stress components at the edges varying with thickness ratio $R_{ht}$ are similar to those of the anti-symmetric shear stress and the symmetric peel stress. In addition, the numerical results also show that, the thinner the

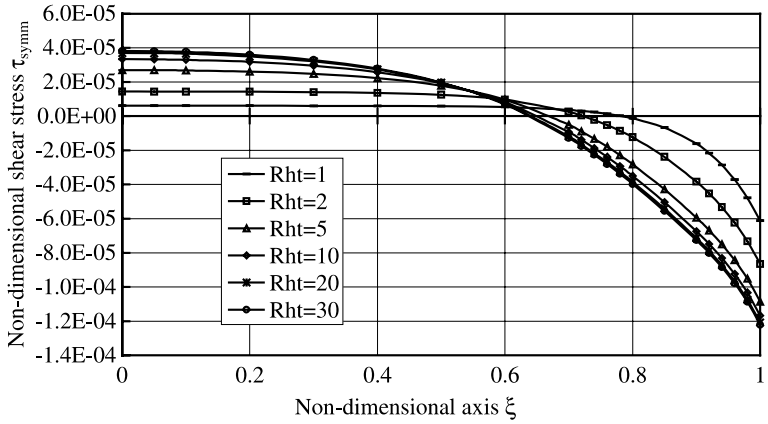


Fig. 23. The symmetric shear stress distribution along half of the PZT patch with $R_{ta} = 10$ and $R_{ht}$ ranging from 1 to 30.

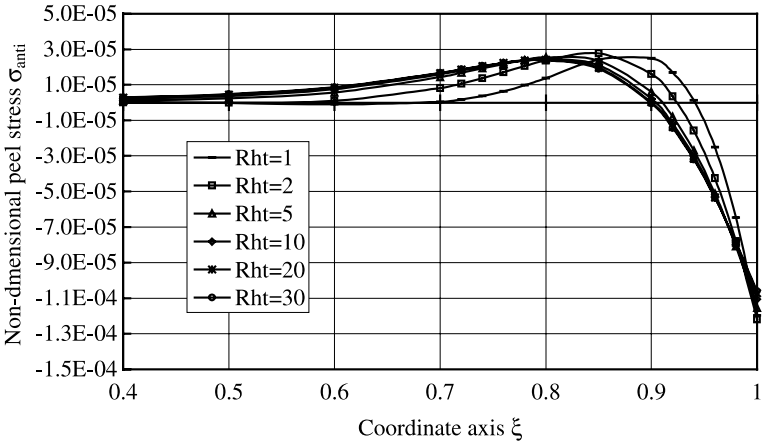


Fig. 24. The anti-symmetric peel stress distribution along 30% of the PZT patch with $R_{ta} = 10$ and $R_{ht}$ ranging from 1 to 30.

adhesive layer, the larger the symmetric shear stress and the anti-symmetric peel stress at the edges. Another point worth noting is that no sensing electric charge is caused by the symmetric shear stress and anti-symmetric peel stress because the integration functions of the electric charge derived by them are odd functions.

Superposing the symmetric and the anti-symmetric components of the shear and peel stresses, we can see that, the shear and peel stresses are very small at $\xi = 1$ and are almost double at $\xi = -1$ for $\alpha_L = 1$. If the shear force is located at the other point of the host beam, the anti-symmetric shear stress and the symmetric peel stress are found by multiplying the value of $\alpha_L$ and the symmetric shear stress and the anti-symmetric peel stress are not related to $\alpha_L$; therefore, the symmetric shear stress and the anti-symmetric peel stress can be neglected when the shear force is loaded far away from the short PZT patch.

### 5.2. The edge debonding

Whether the PZT is used as an actuator or sensor, the shear and peel stresses are concentrated in the PZT edges. When the maximum stress is larger than the bonding strength, the edge debonding of the PZT may develop. The present exact solution can be tailored to the PZT edge debonding by using a shortened bonding length. The actuated stresses at the edge versus the bonding length are plotted in Figs. 25 and 26, which indicate that the shear and peel stresses at the edge remain the same values for the shorter debonding length. It can be shown that the maximum forces also remain the same in this case. If the PZT actuator is used to the structural shape control, the shape will almost maintain the same in this case. However, when the debonding continues developing, the bonding edge stresses will decrease. When the edge stresses decrease to the values below the bonding strength, the debonding will stop by self. This mechanism is the self-arresting behavior, which is the same as that concluded by Wang and Meguid (2000).

Seeley and Chattopadhyay (1999) presented a finite element model that contains the PZT debonding using a refined higher order interpolation function. They concluded that the debonding length is a critical factor; increase in debonding length introduces local and global deformations which have a significant effect on the mode shapes and frequencies. We only consider effects of the debonding length on static behaviors here. Figs. 27 and 28 show the stress redistributions after debonding, in which the distributions of the shear and peel stresses are plotted for the effective bonding length, which is equal to the original PZT length minus the debonding length. Both figures indicate that, the longer the debonding length, the more stresses distributes in the middle zone.

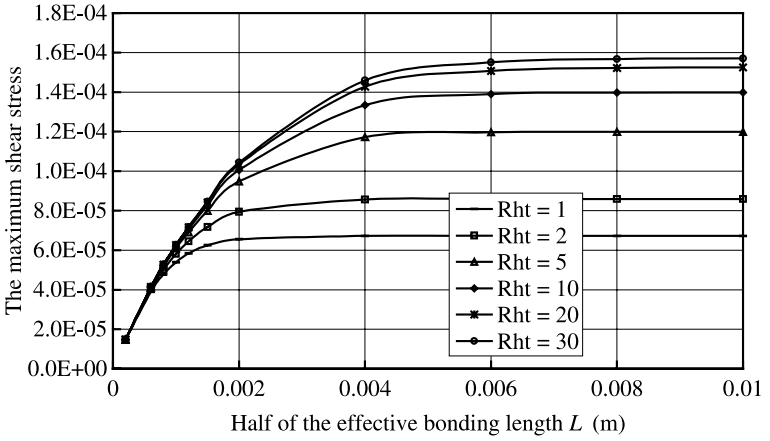


Fig. 25. The shear stress at $\xi = 1$ versus the effective bonding length $L$ with $R_{ta} = 10$ and $R_{ht}$ ranging from 1 to 30.

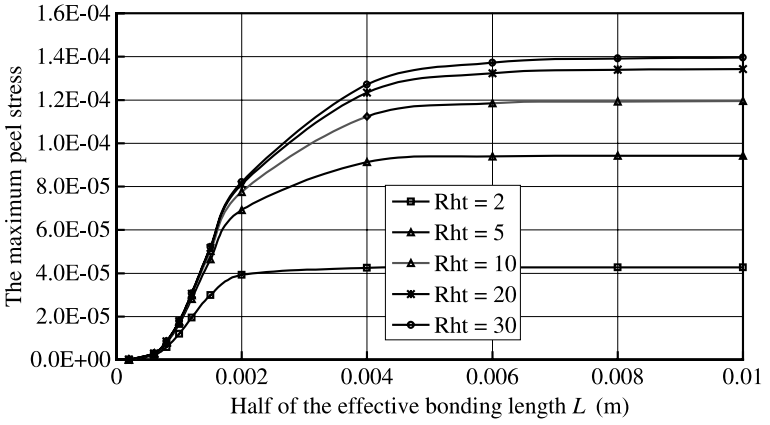


Fig. 26. The peel stress at $\xi = 1$ versus the effective bonding length $L$ with $R_{ta} = 10$ and $R_{ht}$ ranging from 1 to 30.

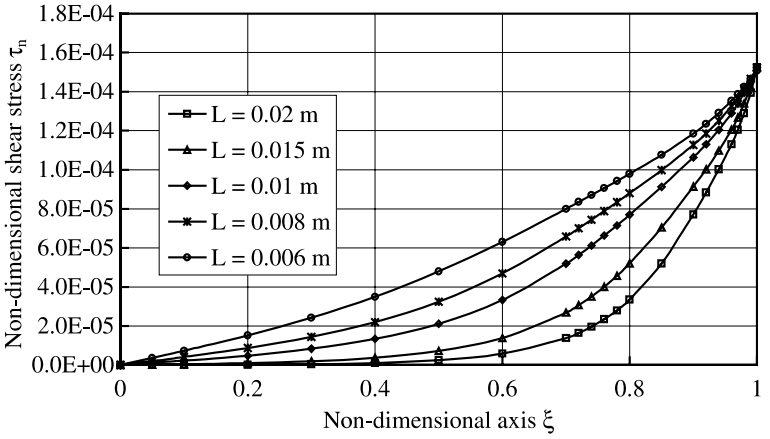


Fig. 27. The shear stress redistribution after debonding with $R_{ta} = 10$ and $R_{ht} = 20$.

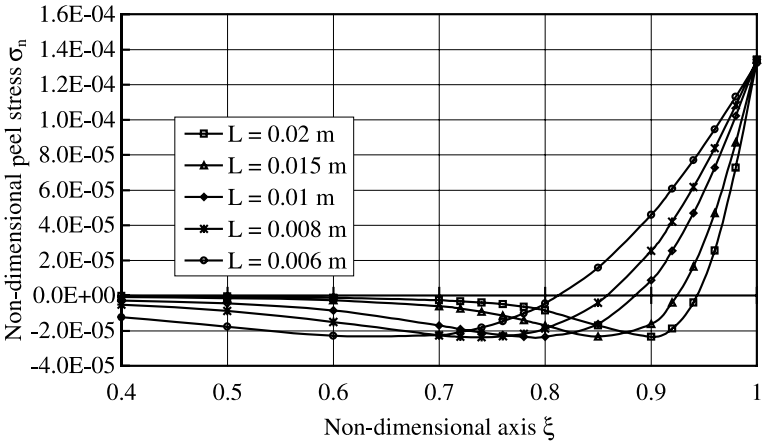


Fig. 28. The shear stress redistribution after debonding with $R_{ta} = 10$ and $R_{ht} = 20$.

## 6. Conclusion

In the numerical result part, the stress distributions, stress resultants and performance of the PZT actuators and sensors are presented and compared with those using the shear lag model. The actuated stress resultants and the sensing charges are in good agreement with those obtained using the shooting method, which validates the exact solutions. The salient points of this paper include:

(1) The present exact solutions take into account the peel stress in the adhesive and provide a more accurate modelling of the smart beams comparing to the shear lag model.
(2) When the host beam deforms extensionally, the present exact solutions correlate well with those obtained using the shear lag model. In this case, the deflection of a PZT patch is very small; therefore, the PZT patch may be modelled as a rod deforming longitudinally and the peel stress may be neglected.
(3) When the host beam deforms in bending, the present results correlate with those predicted by the shear lag model only for the case when the thickness of the host beam is much larger than that of PZT. However, when the host beam-to-PZT patch thickness ratio $R_{ht}$ is small, say $R_{ht} < 5$, large deflection of the PZT patch is observed; therefore, the PZT patch must be modelled as a beam and the peel stress must be included.
(4) When a shear force is applied to the host beam, the shear and peel stresses consist of a symmetric and an anti-symmetric component, and thus the stress distributions are different from those caused by an electric field, an axial force and a bending moment.
(5) The present exact solutions are the general expressions for the smart beam with the bonded PZTs, which can be tailored to solve the PZT edge debonding problem.
(6) The present formulations of the equivalent stress resultants are derived in light of considering the bending behavior of PZTs and are more accurate.

## Acknowledgements

The authors are grateful to the support of the Australian Research Council through a Large Grant Scheme (Grant no. A10009074), and Dr. D. Sun for sharing his numerical results obtained using the shooting method and helpful technical discussions.

## References

Luo, Q., Tong, L., 2002. Exact static solutions to piezoelectric smart beam including peel stress. Part I: theoretical formulation. International Journal of Solids and Structures 39, 4677–4695.

Crawley, E.F., de Luis, J., 1987. Use of piezoelectric actuators as elements of intelligent structures. AIAA Journal 25 (10), 1373–1385.

Goland, M., Reissner, E., 1944. The stresses in cemented joints. Journal of Applied Mechanics, A-17–A-27.

Robbins, D.H., Reddy, J.N., 1991. Analysis of piezoelectrically actuated beams using a layer-wise displacement theory. Computers and Structures 41 (2), 265–279.

Seeley, C.E., Chattopadhyay, A., 1999. Modeling of adaptive composites including debonding. International Journal of Solids and Structures 36, 1823–1843.

Tong, L., Steven, G.P., 1999. Analysis and Design of Structural Bonded Joints. Kluwer Academic, Boston.

Tong, L., Sun, D., Atluri, S.N., 2001. Sensing and actuating behaviors of piezoelectric layer in smart beams with debonding. Smart Materials and Structures 10 (4), 713–723.

Wang, B.T., Rogers, C.A., 1991. Modeling of finite-length spatially-distributed induced strain actuators for laminate beams and plates. Journal of Intelligent System and Structures 2, 38–58.

Wang, X.D., Meguid, S.A., 2000. On the electroelastic behavior of a thin piezoelectric actuator attached to an infinite host structure. International Journal of Solids and Structures 37, 3231–3251.